

## Article

# The Application of Combined Visible and Ultraviolet Irradiation to Improve the Functional Characteristics of Gas Sensors Based on ZnO/SnO<sub>2</sub> and ZnO/Au Nanorods

Alexandra P. Ivanishcheva <sup>1,2,\*</sup>, Victor V. Sysoev <sup>3,\*</sup> , Khabibulla A. Abdullin <sup>4</sup>, Andrey V. Nesterenko <sup>2</sup>, Soslan A. Khubezhov <sup>2,5,6</sup>  and Victor V. Petrov <sup>1</sup> 

- <sup>1</sup> Institute of Nanotechnologies, Electronics, and Equipment Engineering, Southern Federal University, 347928 Taganrog, Russia
- <sup>2</sup> Research Laboratory of Functional Nanomaterials Technology, Southern Federal University, Shevchenko St. 2, 347922 Taganrog, Russia
- <sup>3</sup> Department of Physics, Yuri Gagarin State Technical University of Saratov, 410054 Saratov, Russia
- <sup>4</sup> National Nanotechnology Laboratory of Open Type, Al Farabi Kazakh National University, Almaty 050044, Kazakhstan
- <sup>5</sup> Core Shared Research Facility «Physics and Technology of Nanostructures», North Ossetian State University, 362025 Vladikavkaz, Russia
- <sup>6</sup> School of Physics and Engineering, ITMO University, 191002 St. Petersburg, Russia
- \* Correspondence: starnikova@sfned.ru (A.P.I.); vssysoev@sstu.ru (V.V.S.); Tel.: +7-863-437-1624 (A.P.I.)

**Abstract:** Arrays of zinc oxide (ZnO) nanorods were synthesized over quartz substrates by the hydrothermal method. These nanorods were grown in a predominantly vertical orientation with lengths of 500–800 nm and an average cross-sectional size of 40–80 nm. Gold, with average sizes of  $9 \pm 1$  nm and  $4 \pm 0.5$  nm, and tin nanoclusters, with average sizes of  $30 \pm 5$  nm and  $15 \pm 3$  nm, were formed on top of the ZnO nanorods. Annealing was carried out at 300 °C for 2 h to form ZnO/SnO<sub>2</sub> and ZnO/Au nanorods. The resulting nanorod-arrayed films were comprehensively studied using X-ray diffraction (XRD), scanning electron microscopy (SEM), energy-dispersive X-ray spectrometry (EDS) and X-ray photoelectron spectroscopy (XPS). To fabricate resistive sensor elements, the films were supplied with V/Ni contact metallization on top of the nanorods. The gas sensor performance of the prepared films was evaluated at various temperatures in order to select 200 °C as the optimum one which enabled a selective detection of NO<sub>2</sub>. Adding UV-viz irradiation via a light-emitting diode,  $\lambda = 400$  nm, allowed us to reduce the working temperature to 50 °C and to advance the detection limit of NO<sub>2</sub> to 0.5 ppm. The minimum response time of the samples was 92 s, which is 9 times faster than in studies without exposure to UV-viz radiation.

**Keywords:** ZnO; nanorods; gas sensor; electrophysical properties; NO<sub>2</sub>



**Citation:** Ivanishcheva, A.P.; Sysoev, V.V.; Abdullin, K.A.; Nesterenko, A.V.; Khubezhov, S.A.; Petrov, V.V. The Application of Combined Visible and Ultraviolet Irradiation to Improve the Functional Characteristics of Gas Sensors Based on ZnO/SnO<sub>2</sub> and ZnO/Au Nanorods. *Chemosensors* **2023**, *11*, 200. <https://doi.org/10.3390/chemosensors11030200>

Academic Editor: Boris Lakard

Received: 31 January 2023

Revised: 14 March 2023

Accepted: 17 March 2023

Published: 20 March 2023



**Copyright:** © 2023 by the authors. Licensee MDPI, Basel, Switzerland. This article is an open access article distributed under the terms and conditions of the Creative Commons Attribution (CC BY) license (<https://creativecommons.org/licenses/by/4.0/>).

## 1. Introduction

The most common materials used to fabricate gas sensors are nanocomposite films or nanostructures based on semiconducting metal oxides [1,2]. To improve the characteristics of gas sensors, including sensitivity, selectivity, operating temperatures, temporal stability and energy efficiency, and to reduce the cost of production for systems of continuous emission control and monitoring, intensive efforts are being made to develop efficient methods for the synthesis and modification of nanostructured materials [3]. Excellent results have been demonstrated by nanocomposite materials based on MXenes [4]. Their sensitivity to nitrogen dioxide (NO<sub>2</sub>) is at the level of tens of ppb and their reaction rate is not worse than units of a second [5]. However, their disadvantages are their complex structure, unexplored mechanism of gas sensitivity and low the long-term stability [6]. Gas sensors based on heterojunctions between oxides of different metals or between metal and metal oxides are found to be highly sensitive [7]. Zinc oxide (ZnO) is a promising metal

oxide that is widely used as a sensing layer in chemiresistive sensors [8]. A variety of technologies have been considered for the production of nanostructured ZnO due to the fast growth of the crystals in certain directions under a controlled environment. Among many approaches, the low-cost and low-temperature protocols are the most interesting [9].

One way to increase the selectivity of semiconductor oxides is to modify their surface with metal nanoparticles such as Au [10]. The use of Au nanoparticles yields options for promoting the selectivity of the sensor toward gases such as CO, H<sub>2</sub> and NO<sub>2</sub> because the gold can catalyze the surface reactions upon the gas adsorption due to the spillover effect [11,12]. Gas sensors based on ZnO/Au and ZnO/Sn nanocomposites are becoming an object of high interest [13–16].

Another way to increase the sensitivity and selectivity of semiconductor oxides is by designing nanocomposite structures and materials containing heterojunctions of two metal oxides, for example ZnO/In<sub>2</sub>O<sub>3</sub> [17,18], ZnO/SnO<sub>2</sub> [19–21] or TiO<sub>2</sub>/SnO<sub>2</sub> [22]. The formed heterojunctions increase the lifetime of electron–hole pair carriers by eliminating recombination processes which enhance redox reactions when exposed to analyte [23].

The operating temperatures of gas sensors based on semiconducting metal oxides are ordinarily in the range of 200–450 °C [24,25]. High temperatures cause a short warranty period for sensor operations, as sensors need to function continuously for a long time. There is a significant amount of work to show that gas sensitivity processes are well-activated by ultraviolet radiation, which helps us reduce the operating temperature of gas sensors; not only their sensitivity but also their selectivity to gases is significantly improved [26–29]. The comprehensive reviews that have recently been published discuss the principles of operation for resistive semiconductor gas sensors upon excitation by a light activation instead of thermal heating when detecting gases [23]. They also describe the results of the utilization of photoactivated nanomaterials (nanostructures, hybrids of metal oxide semiconductors and two-dimensional materials) in the gas-sensing field [26,27].

Nitrogen dioxide is a toxic gas that has a negative impact on human health and the environment [30,31]. Chemiresistive sensors are being considered as a potential solution to enable inexpensive monitoring of atmospheric NO<sub>2</sub>, and, therefore, they are attracting considerable attention in research [32]. Nanostructured ZnO is widely employed in the fabrication of chemiresistive sensors, thanks to its significant conductivity on surface processes and its excellent chemical and thermal stability.

It is widely shown in the literature that unmodified ZnO films and nanostructures (nanofibers, nanorods, nanosheets, etc.) exhibit high sensitivity to NO<sub>2</sub> and other gases, frequently with detection limits below 1 ppm during heating of higher than 200 °C [33–36]. Modification of ZnO nanofilms and nanostructures by foreign elements, such as gold or tin oxide, can lead to a significant increase in their sensitivity and selectivity, although the operating temperature decreases slightly [37–39]. When applying UV activation to pristine ZnO films and nanostructures, these sensors exhibit a high sensitivity to NO<sub>2</sub> concentrations of 1–10 ppm when the NO<sub>2</sub> is already at room temperature or close to it [23,40]. Recently, a similar trend was shown for the use of UV-activated ZnO that was decorated with gold and tin oxide to improve the detection limit of NO<sub>2</sub> and the response to it [41,42].

It should be noted that the intensity of the UV power density on gas-sensitive materials is a very important parameter. The greater the intensity of the radiation, the higher the response obtained [42,43]. However, powerful UV radiations might contribute to the dissociation of NO<sub>2</sub> molecules [44]. This, in turn, leads to uncertainties in the measurements. In this regard, it is important to use LEDs with a controlled low-radiant intensity of no higher than 500 μW/cm<sup>2</sup>.

Recently, we developed nitrogen dioxide sensors based on zinc oxide NRs with Sn and Au gold clusters [37,45]. We found that the response of sensors based on ZnO/Sn NRs, at an operating temperature equal to 200 °C and when exposed to NO<sub>2</sub> at a concentration of 50 ppm, was about 47.3, while ZnO/Au NR sensors yielded the response of ca. 40.6. At an operating temperature of 150 °C, the response of these sensors was reduced to 9.6 and 8.3,

respectively. Still, at both temperatures, the response and recovery times were longer than 1100 s. To reduce the operating temperature, additional activation was implemented using a light-emitting diode (LED) with a wavelength of 400 nm and whose spectrum included a UV range with a power density incident irradiance of  $133 \mu\text{W}/\text{cm}^2$ .

Thus, the purpose of this work was to investigate the effects of exposing ZnO NRs modified with Au or Sn to high temperatures and UV-viz radiation simultaneously ( $133 \mu\text{W}/\text{cm}^2$ ) in order to reduce the operating temperatures and response times of the sensors while ensuring a high sensitivity to  $\text{NO}_2$  gas.

## 2. Materials and Methods

### 2.1. Materials

Quartz substrates, zinc acetate  $\text{Zn}(\text{CH}_3\text{COO})_2$ , zinc nitrate  $\text{Zn}(\text{NO}_3)_2 \cdot 6\text{H}_2\text{O}$  and hexamethylenetetramine ( $(\text{CH}_2)_6\text{N}_4$ ) (Sigma-Aldrich, Merck, Chengdu, China) were used to synthesize ZnO NRs. Prior syntheses, with substrates of  $20 \times 40 \times 0.5 \text{ mm}^3$ , were thoroughly cleaned in a detergent solution and dried under normal air conditions. For uniform synthesis of the substrate and strong adhesion of the output oxide layer, ZnO seeds were primarily deposited using the sol-gel method. The sol was obtained by dissolving approx. 1 mg of zinc acetate  $\text{Zn}(\text{CH}_3\text{COO})_2$  in 10 mL of ethanol at RT. A few drops of the sol solution were applied to a substrate for centrifugation with a rotational speed of up to about 2000 rpm for 1 min. After that, the substrates were dried in a desiccator for 30 min at  $110 \text{ }^\circ\text{C}$ . To obtain the ZnO layers, the substrates, equipped with thin, uniform layers of zinc acetate, were air annealed in a muffle furnace at  $350 \text{ }^\circ\text{C}$  for 60 min. The typical thickness of the ZnO seed layer was about 30 nm [46,47].

The ZnO NR layers were synthesized by the chemical bath deposition (CBD) method. The substrates with the seed layer were placed vertically in a glass beaker, facing the center and fixed on the upper edge of the beaker with a one-sided polyimide adhesive tape. An aqueous 0.05 M equimolar solution of  $\text{Zn}(\text{NO}_3)_2 \cdot 6\text{H}_2\text{O}$  and  $(\text{CH}_2)_6\text{N}_4$  was utilized during the synthesis. The beakers with the substrates, and magnetic anchors, were filled up to 2/3 of their height with this solution and placed in a water bath with a magnetic stirrer. The synthesis was carried out at  $94\text{--}95 \text{ }^\circ\text{C}$  for approx. 1 h. After the synthesis, the samples were taken out, washed with distilled water in an ultrasonic bath to remove the surface impurities, and dried in a desiccator [48].

### 2.2. Modification of Materials

Thin layers of metals (Au and Sn) with 0.999 purity were deposited on the surface of the ZnO NR arrays using thermal vacuum evaporation (VUP-5M, JSC «SELMI», Sumy, Ukraine), with the unit pumped down to approx. 20 mPa and a nitrogen trap employed. A sample of about 10 mg of metal was placed on a tungsten evaporator with the substrate, which contained an array of ZnO NRs, to be distanced by approx. 10 cm. The thickness of the sputtered layer was estimated from the known weight of the suspension, the distance from the suspension to the target and the metal density. The calculations (Supplementary Materials) showed that the sizes of the tin and gold nanoclusters were close to the thickness of the deposited layer. We developed three series of samples of ZnO NR arrays with gold nanocluster sizes of  $9 \pm 1 \text{ nm}$  (sample ZnO/Au(1)) and  $4 \pm 0.5 \text{ nm}$  (sample ZnO/Au(2)). A similar number of samples was obtained by tin sputtering. For the tin, the calculated nanocluster sizes were  $30 \pm 5 \text{ nm}$  (sample ZnO/SnO<sub>2</sub>(1)) and  $15 \pm 3 \text{ nm}$  (sample ZnO/SnO<sub>2</sub>(2)). Finally, the substrates with ZnO/Au and ZnO/SnO<sub>2</sub> NRs were cut into separate samples of  $5 \times 5 \text{ mm}^2$  for further studies. Since the gas-sensitive properties of resistive gas sensors are manifested at high temperatures, XPS studies were carried out on samples that were heated at 200 and  $300 \text{ }^\circ\text{C}$  for 120 min. For the manufacture of resistive sensor elements and electrophysical measurements, V/Ni contact metallization was formed on top of ZnO/SnO<sub>2</sub> and ZnO/Au nanorods, resulting in electrodes that were 0.3–0.4 mm thick and distanced at 500  $\mu\text{m}$  from each other.

### 2.3. Characterization

The resulting ZnO NRs were comprehensively studied using X-ray diffraction (XRD), scanning electron microscopy (SEM), energy-dispersive X-Ray spectrometry (EDS) and X-ray photoelectron spectroscopy (XPS).

The structural properties of the synthesized materials were studied using XRD with the help of an ARL X'TRA diffractometer («Thermo Fisher Scientific SARL», Ecublens, Switzerland) using CuK $\alpha$  radiation, wavelength  $\lambda = 0.1540562$  nm.

SEM studies were performed with the Nova 600 NanoLab (FEI Company, Hillsboro, OR, USA), which combines the microscopy at ultrahigh resolution using the EDS detector Genesis 600i (EDAX, Ametek, The Netherlands).

The XPS studies were carried out with the ThermoScientific K-Alpha spectrometer (model IQLAADGAAFFACVMAHV, Waltham, MA, USA) by employing AlK $\alpha$  monochromatic rays with 1486.6 eV of energy and spot sizes of 400  $\mu$ m. High-resolution spectra were obtained using a constant analyzer energy with a pass energy of 20 eV and a spectral resolution of 0.1 eV. The binding energy of the Au4f photoelectrons collected from the gold reference sample was equal to 84 eV. Because the gas-sensitive properties of the material in the resistive gas sensors under study are manifested at high temperatures, XPS studies were carried out on samples heated at 200 °C and 300 °C for 120 min.

The I-V curves and electrical conductivity of the samples were recorded at different operating temperatures with the help of a PC-driven setup described elsewhere [49]. The activation energy of conductivity,  $E_a$ , was estimated by the Arrhenius equation (Equation (1)) [50]:

$$G = G_0 \cdot \exp(-E_a/k \cdot T), \quad (1)$$

where  $k$  is the Boltzmann constant and  $G_0$  is a coefficient accounting for the bulk material conductivity.

Next, the temperature-stimulated conduction measurements were performed according to previously developed protocols [51,52] in order to evaluate the effective value of the energy barrier between the grains of the nanocrystalline material.

The gas response of the sensors to concentrations of 0.5–50 ppm of nitrogen dioxide, balanced with synthetic air, was measured at operating temperatures in the range of 50–200 °C. High-pressure balloons containing synthetic air, a N<sub>2</sub>/O<sub>2</sub> mixture and a mixture of synthetic air with NO<sub>2</sub> (Monitoring LLC, St. Petersburg, Russia) were employed as the primary sources. The gases were injected at a flow rate of 0.3 dm<sup>3</sup>/min using a gas-mixing generator (Microgaz F, Moscow, Russia) [49]. The sensors were initially exposed to the air for 60 min. to stabilize the baseline resistance. The response of the sensor elements was calculated using Equation (2):

$$S = R_g/R_0, \quad (2)$$

where  $R_0$  and  $R_g$  are the sensor resistances in synthetic air and the mixture of synthetic air and NO<sub>2</sub>, respectively. Subsequently, the gas sensor which exhibited the best gas-sensing performance was tested upon exposure to NO<sub>2</sub>.

In order to study the parameters of the photoconductivity of ZnO NR heterostructures formed on opaque substrates, we applied a custom-fabricated setup containing an LED (GNL-3014VC, «G-nor Electronics», Zhuangshi, China) with a wavelength of 400 nm. The CENTER 532 UV intensity meter (Center Light Technology Limited, Center, model 532, Xixiang Town, Baoan District, Shenzhen, China) and a CENTER 530 illuminance meter (Luxmeter, model 530, Xixiang Town, Baoan District, Shenzhen, China) were used to measure the parameters of the LED radiation. Prior to the measurement of the photoconductivity and gas-sensitive properties of the films, a counter-pin contact V-Ni metallization of 300 nm thick was sputtered using thermal vacuum evaporation through a mask to design a planar resistor with an initial resistance of  $R_0$ . For this purpose, the substrate containing the nanocomposite material was placed on a heating platform to heat the film up to 300 °C. The photoconductivity was monitored with a Tektronix DMM 4050 digital multimeter (Tektronix, Beaverton, OR, USA). Direct measurements were carried out to find

the photoconductivity under the influence of the light emitted from the LED; the level of visible light on the sample was equal to 525 lux, and the power density of the UV radiation was equal to  $133 \mu\text{W}/\text{cm}^2$ . These studies of the photoconductivity allowed us to specify the time parameters required to measure the gas-sensitive properties of arrays of ZnO/Au and ZnO/SnO<sub>2</sub> NRs to NO<sub>2</sub> under heating and UV-viz radiation.

### 3. Results and Discussion

#### 3.1. Structural, Morphological and Compositional Characteristics

The results of the X-ray analysis (Figure 1) showed that the ZnO NRs had a wurtzite structure [52] with a preferential growth along the (002) direction.

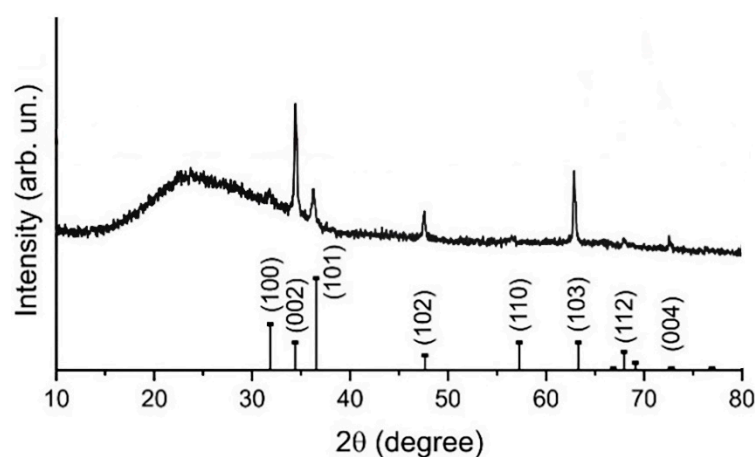


Figure 1. XRD patterns of the ZnO NR array samples synthesized by the CBD method.

Electron microscopic studies of arrays of pristine ZnO NRs prior to metal sputtering revealed that the nanorods had an almost vertical orientation, an average transverse size of 40–80 nm and lengths of 500–800 nm; see Figure 2. An area of  $1 \times 1 \mu\text{m}^2$  contains approx. 160 rods.

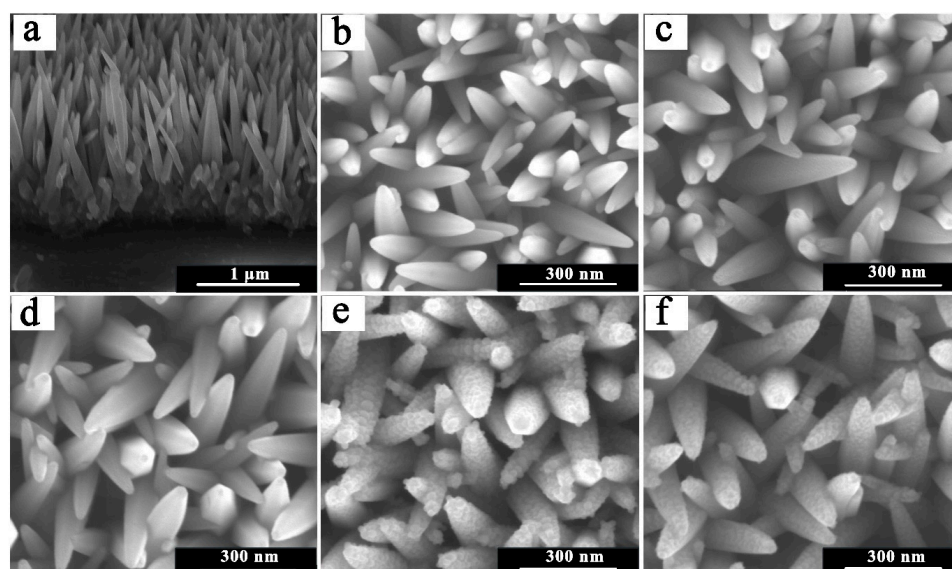
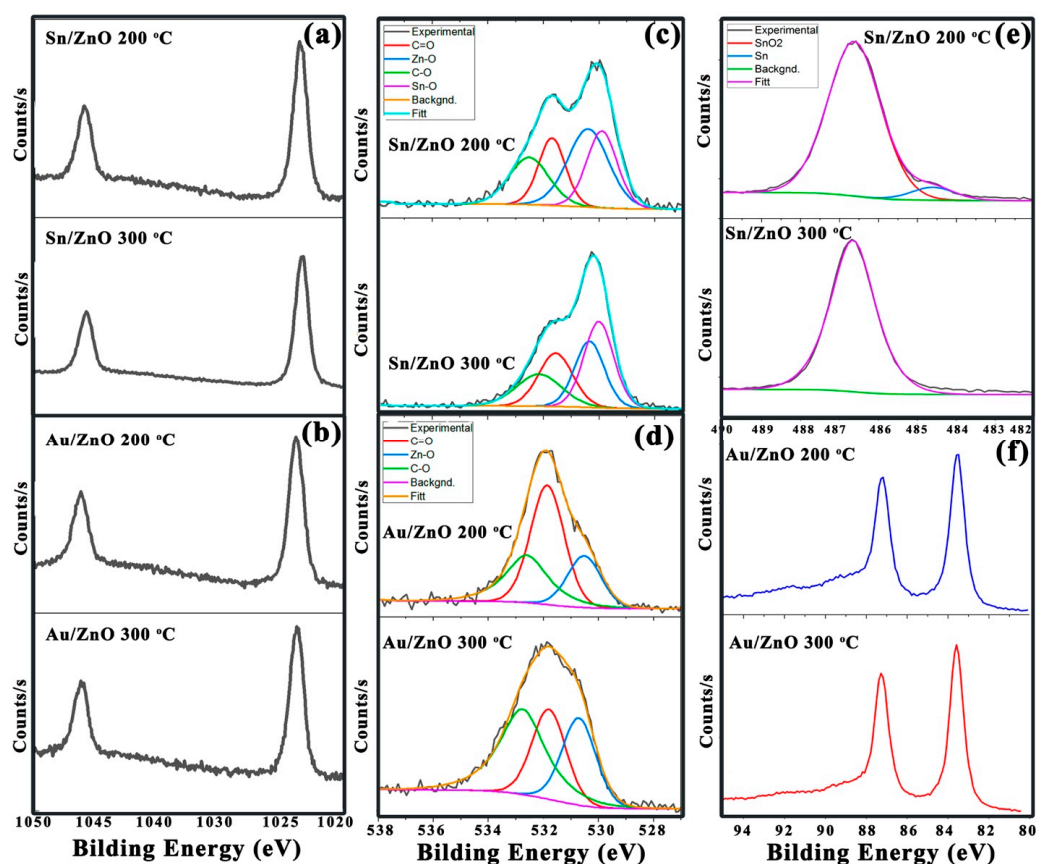


Figure 2. SEM images of the ZnO NRs on the sensor substrate: (a,b) pristine ZnO NRs at (a) cross-section and (b) top view; (c) ZnO/Au(1) NRs; (d) ZnO/Au(2) NRs; (e) ZnO/SnO<sub>2</sub>(1) NRs; (f) ZnO/SnO<sub>2</sub>(2) NRs.

Figure 2c,d shows that the vacuum thermal spraying resulted in the fabrication of gold and tin nanoclusters over the ZnO NRs. The figure proves that these nanoclusters were evenly arranged over the entire surface of the ZnO NR array.

### 3.2. XPS Analysis

From the analysis of the high-resolution spectra of the C1s photoelectron lines (Supplementary Materials, Figure S1), it is clear that the shapes of the curves and the positions of the intensity maxima fully correspond to the data in the literature concerning atmospheric carbon with characteristic C-C bonds (284.8 eV), C-O (286.2 eV) and C=O (288.4 eV) [53]. Increasing the annealing temperature led to significant changes in the C-C component intensity and the C-O/C=O component intensity and the C-O/C=O component ratio, especially for the ZnO/Sn NR sample. It can be assumed that the desorption of carbon adsorbate from the sample surfaces has a different character as a result of the annealing from the surfaces of the ZnO/Au and ZnO/Sn NRs. The ZnO/Au NRs were represented as a simple thermal desorption, while in the case of the ZnO/Sn NRs, it involved a redox processes. Figure 3a,b,f shows that the shape and positions of the photoelectron spectra of Au4f (83.5 eV) and Zn2p (1021.4 eV) did not change depending on the annealing temperature of the ZnO/Au NRs. However, in contrast to the Au4f spectra, where the photoelectron signal amplitude went up with increases in the annealing temperature, the Zn2p spectra exhibited a reduction in the intensity of the peaks. This fact can be explained by the way the surface rearranged the Au nanoparticles into nanoclusters which, in turn, led to the partial screening of the Zn photoelectronic signal to be relayed to the free path length of the electron [54].



**Figure 3.** XPS characterizations of ZnO/Au and ZnO/Sn NR samples after annealing at 200 °C and 300 °C: (a,b) high-resolution spectra of (a) Zn2p in ZnO/Sn NR and (b) ZnO/Au NR; (c,d) high-resolution O1s spectra in (c) ZnO/Sn NR and (d) ZnO/Au NR; (e) high-resolution Sn 3d spectra in ZnO/Sn NR; and (f) high-resolution Au4f spectra in ZnO/Au NR.

The analysis of the high-resolution photoelectron lines of O1s spectra (Figure 3c,d) qualitatively agrees and confirms our assumptions about the mechanisms of desorption and the redox processes that occurred in the ZnO/Sn NRs and clustering Au nanoparticles in the ZnO/Au NRs under heating. Thus, Figure 3c reveals that the annealing of the ZnO/Sn NR results in a significant change in the component ratios, particularly in reducing C-O and C=O and enhancing the metal-oxide components of ZnO and SnO<sub>2</sub>.

The increase in the intensity of the Sn-O component in the O1s spectrum (Figure 3c) can be explained, on the one hand, by desorption of carbon from the surface of the ZnO/Sn NRs, and, on the other hand, by the oxidation of the tin. The latter was verified by analyzing the high-resolution spectra of the Sn3d peaks (Figure 3e). Indeed, one can see that the sample annealed at 200 °C had both an oxide and a metallic component, with binding energies of 486.6 eV and 484.7 eV, respectively [54]. At the same time, it should be noted that, unlike the spectra of the ZnO/Au NR, the intensity of the photoelectron signal of the Zn2p enlarged with a higher annealing temperature (Figure 3a). This is due to both the desorption of carbon and the formation of tin oxide. The key here is the appearance of the tin oxide, which led to the enhancement of the free path length of the photoelectron and, as a consequence, increased the depth of the near-surface layer analysis by the XPS method [55]. Thus, after annealing at 300 °C, the gold in ZnO/Au NRs remained in the metallic state, but the tin converted to tin dioxide while forming a ZnO/SnO<sub>2</sub> heterojunction. Subsequently, before measurements were taken, all structures were annealed at 300 °C for two hours to stabilize the parameters.

### 3.3. Electrical Characterization

Following preparation, the ZnO/Au and ZnO/SnO<sub>2</sub> NR-based sensors were annealed in air at 300 °C for 2 h to stabilize the electrophysical characteristics of the formed materials. Figure 4 plots the resistivity (R) of the studied samples on the operating temperature.

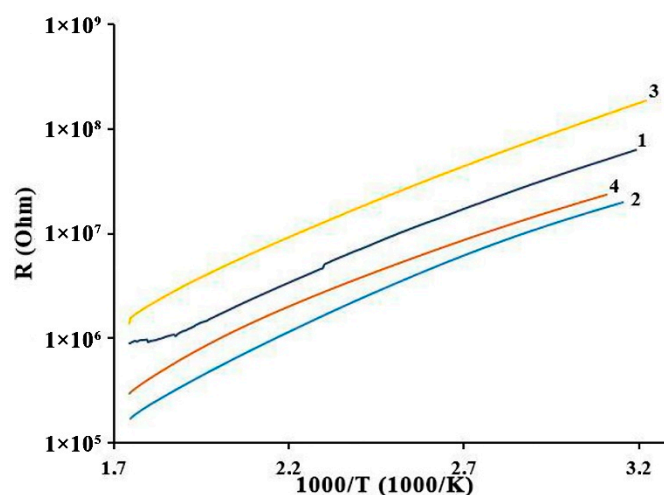


**Figure 4.** Dependence of resistance (R) on the operating temperature (T) of samples ZnO/SnO<sub>2</sub> (1) (1), ZnO/SnO<sub>2</sub> (2) (2), ZnO/Au(1) (3) and ZnO/Au(2) (4) NRs.

As one can see, the temperature dependences of the sample resistance of the obtained samples followed a linear function. In the sample of the ZnO/Au(1) NR array, the resistance values were an order of magnitude greater than those of ZnO/SnO<sub>2</sub> (2), which seems to be explained by the difference in thickness. Therefore, the sensors based on ZnO NRs required a temperature stabilization because their resistance had a strong dependence on the temperature of the heating.

The activation energy of conductivity ( $E_a$ ) was further evaluated and was calculated based on Equation (1). It was estimated that, in the temperature range of 44–300 °C,  $E_a$  is equal to 0.25–0.27 eV for the ZnO/SnO<sub>2</sub> NR samples and 0.23–28 eV for the ZnO/Au NR samples. These values are similar to the ones observed earlier in nanotubes of titanium

dioxide [56], which shows that their fundamental character to mature is likely due to the nanorod contacts. It is known that the work function of ZnO (5.2–5.3 eV) [57,58] is higher than that of SnO<sub>2</sub> (4.8–4.9 eV) and Au (4.76 eV) [59,60]. When ZnO and SnO<sub>2</sub> crystallites are in contact with each other, electrons transfer from the tin dioxide to the zinc oxide [52]. The same process occurs at the ZnO/Au heterojunction. In this case, a potential barrier  $\varphi_b$  appears and is close in magnitude to the difference in the electron output of materials participating in the heterojunction. For the ZnO/SnO<sub>2</sub> and ZnO/Au heterojunctions,  $\varphi_b$  should be approximately equal to 0.3–0.5 eV. Earlier, we determined that the potential barrier values of the NR samples,  $\varphi_b$ , estimated by thermally stimulated conductivity measurements, were found to be 0.34 eV for ZnO/SnO<sub>2</sub>(1), 0.43 eV for ZnO/SnO<sub>2</sub>(2), 0.34 eV for ZnO/Au(1) and 0.37 eV for ZnO/Au(2) [45]. Thus, the values of potential barriers at the ZnO/SnO<sub>2</sub> and ZnO/Au heterojunctions coincided with the estimated values. The contacts of zinc oxide nanorods and Au(a) and SnO<sub>2</sub> (b) nanocrystallites, as well as the scheme of surface potential formation, are provided in Supplementary Materials (Figure S3).

### 3.4. Photoconductivity Measurements

Figure 5 depicts the behavior of the nanorod sample resistance,  $R_i$ , with a time following 0 s. The resistance values were normalized by the resistance,  $R_0$ , recorded in dark conditions. The measurements were performed until the curves flattened.

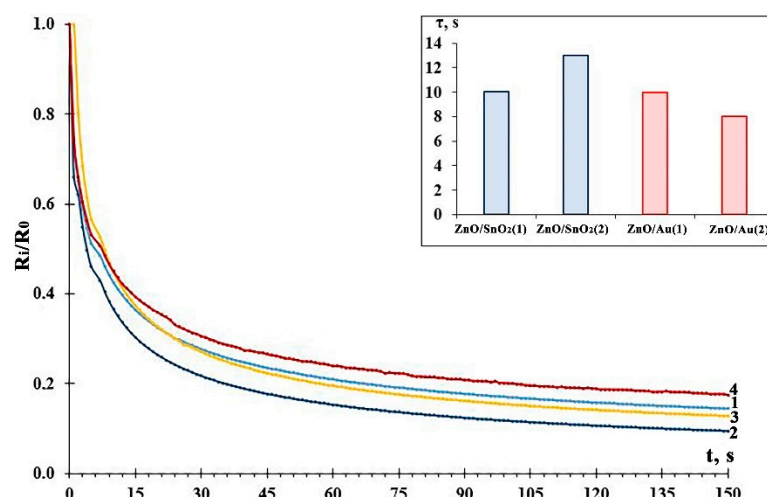


**Figure 5.** The kinetics of resistance of four sensor samples: (1) ZnO/SnO<sub>2</sub> (1), (2) ZnO/SnO<sub>2</sub> (2), (3) ZnO/Au(1) and (4) ZnO/Au(2) NRs, inserting plots of the constants of photoconductivity relaxation time,  $\tau$ , for various samples.

We estimated the time constant of photoconductivity relaxation,  $\tau$ , using Equation (3) [50]:

$$\frac{R_0}{(R_0 - R_i)} = \left(1 - e^{-\frac{t_i}{\tau}}\right), \quad (3)$$

where  $R_0$  is the resistance recorded in dark conditions, and  $R_i$  is the resistance under UV-viz irradiation at  $t_i$ .

These values are presented in the insert of Figure 5. It is evident that the time constants have close values for the different samples to range from 8 to 12 s. The larger values of  $\tau$  correspond to larger values of  $E_a$  and  $\varphi_b$ . This indicates the influence of the activation energy of conductivity and the potential barrier in the zinc oxide NRs on the mechanism of the current transfer. The minimum value of  $\tau$  equal to 8 s was found in the ZnO/Au (2) sample, which had smaller values of  $E_a$  and  $\varphi_b$  than the ZnO/Au (1) sample. These findings also indicate that it is necessary to wait more than 3 min to stabilize the resistance of the gas sensor after turning on the UV-viz irradiation.

### 3.5. Gas Sensor Measurements

Figure 6a,b shows the characteristic  $R(t)$  transients recorded when the ZnO NR samples were exposed to  $\text{NO}_2$  at  $200\text{ }^\circ\text{C}$  without U-viz radiation. For convenience and for comparison, the resistance data were normalized by an initial value of  $R_0$  taken in pure air.

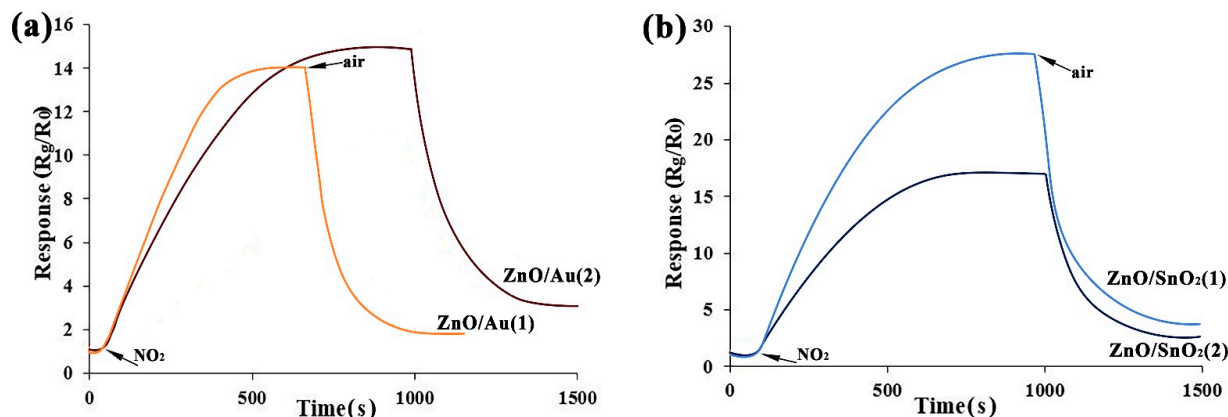


**Figure 6.** The resistance-to-time curves characterizing the responses of (a) ZnO/Au and (b) ZnO/SnO<sub>2</sub> samples at  $200\text{ }^\circ\text{C}$  to  $\text{NO}_2$  with a concentration of 10 ppm. The resistance values are normalized by an initial value of  $R_0$  recorded in background air.

As one can see, when exposed to  $\text{NO}_2$ , the chemiresistive response of the ZnO NR samples,  $S$ , reached 13–14 for the samples of ZnO/Au, while it was equal to 15–26 for the ZnO/SnO<sub>2</sub> samples. Thus, the ZnO/SnO<sub>2</sub> samples had larger responses than the ZnO/Au ones. It appears that the potential barrier arising at the ZnO-SnO<sub>2</sub> heterojunction plays a more significant role than the catalytic ability of the gold nanoclusters on the ZnO surface. However, the response time,  $t_{res}$ , estimated for the resistance to reach 90% saturation was better in the case of the ZnO/Au NR samples, in which it was equal to 540–572 s, than in the ZnO/SnO<sub>2</sub> ones, in which  $t_{res}$  was 610–858 s.

To assess the selectivity of the fabricated sensor structures, the ZnO/SnO<sub>2</sub> and ZnO/Au NR samples were exposed to analyte gases ( $\text{C}_2\text{H}_5\text{OH}$ ,  $\text{NH}_3$ ,  $\text{C}_3\text{H}_8\text{O}$ ,  $\text{C}_3\text{H}_6\text{O}$ ,  $\text{CH}_3\text{OH}$ ) at concentrations of 10 ppm in mixtures with synthetic background air. The obtained values of the chemiresistive responses recorded under the sensor operation at  $200\text{ }^\circ\text{C}$  are summarized in Figure 7.

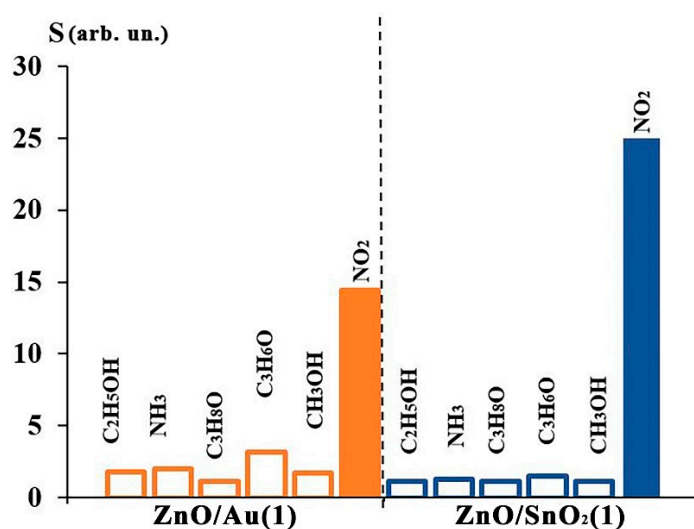


**Figure 7.** The chemiresistive responses of sensors based on ZnO/SnO<sub>2</sub> and ZnO/Au NRs upon exposure to  $\text{C}_2\text{H}_5\text{OH}$ ,  $\text{NH}_3$ ,  $\text{C}_3\text{H}_8\text{O}$ ,  $\text{C}_3\text{H}_6\text{O}$  and  $\text{CH}_3\text{OH}$  at 10 ppm concentration at  $200\text{ }^\circ\text{C}$ .

These data clearly show that the responses of the ZnO/Au and ZnO/SnO<sub>2</sub> NRs to NO<sub>2</sub> were 12–20 times higher than their responses to the other test gases. This indicates that the developed sensors had a high selectivity to nitrogen dioxide. This may be due to the fact that nitrogen dioxide molecules react more quickly with oxygen ions adsorbed on the surface (see Equations (4) and (5)). Therefore, studies on simultaneous exposure of the sensors to gas and UV-viz radiation were carried out on the analyte.

Figure 8 shows the responses of sensors based on the ZnO/Au and ZnO/SnO<sub>2</sub> NRs when exposed to NO<sub>2</sub> in concentrations of 0.5–10 ppm and under heating at 50–150 °C and UV-viz radiation.

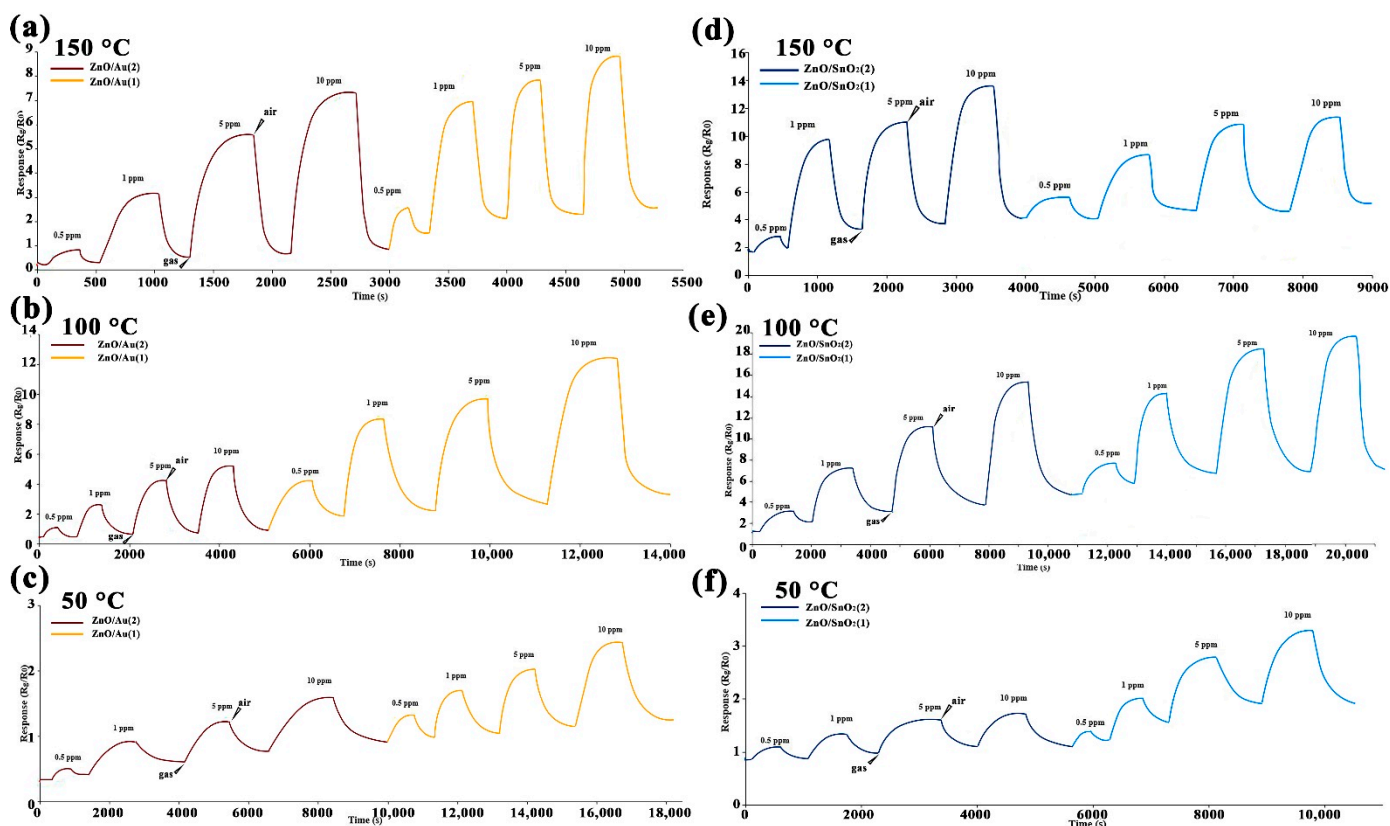


**Figure 8.** The typical  $R(t)$  transients characterizing sensors based on (a–c) ZnO/Au(1) and ZnO/Au(2) and (d–f) ZnO/SnO<sub>2</sub>(1) and ZnO/SnO<sub>2</sub>(2) when exposed to NO<sub>2</sub> at concentrations of 0.5, 1, 5 and 10 ppm and UV-viz radiation after heating to operating temperatures of 50 °C, 100 °C and 150 °C.

The data provided in Figure 8 and Table 1 prove that the samples based on the ZnO/SnO<sub>2</sub> NRs were approx. 1.3–2 times more sensitive to NO<sub>2</sub> than those based on the ZnO/Au NRs, in accordance with data described above. This means that the UV-viz activation does not change the advanced gas-sensing properties of ZnO/SnO<sub>2</sub> NRs. The response times,  $t_{res}$ , were found to be 256–330 s and 553–564 s for the ZnO/Au and ZnO/SnO<sub>2</sub> NR samples when exposed to 10 ppm of NO<sub>2</sub>, which is ca. 1.5–2 times lower than those recorded without UV-viz radiation, as plotted in Figure 6.

Thus, the data presented in Table 1 provide evidence that the sensors based on ZnO/Au NRs in the 100–150 °C temperature range and under UV-viz radiation exhibited lower response time values than the ZnO/SnO<sub>2</sub> NRs. However, the ZnO/SnO<sub>2</sub> sensors had better response times when the operating temperature was reduced to 50–150 °C. This may be due to the magnitude of the potential barrier  $\phi_b$ , which was the largest for this composition. As has been previously established, the oxygen chemisorption defines the magnitude of the potential barrier on the surface of the semiconductor oxide grains [61]; therefore, the higher the magnitude of the potential barrier, the higher the response.

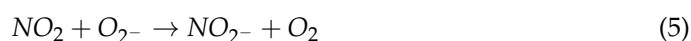
**Table 1.** Chemiresistive response magnitude,  $S$ , and response time,  $t_{res}$ , characterizing sensors based on ZnO/Au and ZnO/SnO<sub>2</sub> NRs exposed to NO<sub>2</sub> under combined conditions of heating and UV-viz radiation.

Material Gas Sensor		Operating Temperature and Concentration of NO <sub>2</sub>											
		50 °C				100 °C				150 °C			
		0.5 ppm	1 ppm	5 ppm	10 ppm	0.5 ppm	1 ppm	5 ppm	10 ppm	0.5 ppm	1 ppm	5 ppm	10 ppm
ZnO/Au(1)	$S$	1.5	1.9	2.2	3	4.3	6.4	7.5	9	2.5	4.7	6	6.5
	$t_{res}$	519	632	741	1087	744	722	820	931	92	289	232	256
ZnO/Au(2)	$S$	1.3	1.6	1.7	2.5	1.5	2.2	3.6	4	1.7	3.8	5	6.7
	$t_{res}$	508	1127	1071	1522	243	422	495	520	234	416	390	330
ZnO/SnO <sub>2</sub> (1)	$S$	1.4	1.8	1.5	2	3	8.5	11.5	13	2.4	4.8	6	6.3
	$t_{res}$	507	510	684	584	851	919	1147	957	550	658	815	564
ZnO/SnO <sub>2</sub> (2)	$S$	1.7	2.3	3	3.3	2.7	5	8	12	2	7.6	7.7	9.8
	$t_{res}$	395	527	771	696	1045	1182	1123	1185	389	435	475	553

The gas-sensing properties of the ZnO NR-based sensors are well explained in the framework of the electron-depleted layer (EDL) model [55]. When the sensor is exposed to air at temperatures below 200 °C, oxygen molecules are adsorbed on the surface of sensitive materials, and electrons are captured from the conduction zone to form ion species  $O_2^-$  [56], as shown in Equation (4). These processes lead to an at-surface electron-depleted layer and narrow the conductive channel, as described, for instance, in [62,63].



When sensors are exposed to NO<sub>2</sub>, the chemisorbed oxygen reacts with the NO<sub>2</sub> according to Equation (5) [62]:



This reaction reduces the concentration of oxygen ions on the surface of the ZnO NRs and accelerates the reaction. This increases the EDL thickness and, consequently, results in a higher overall resistance of the gas sensor.

Furthermore, the UV-viz radiation with an energy level of 3.1–3.4 eV corresponds to the ZnO gap, equal to 3.37 eV [64], which allows one to generate additional free electrons in this wide-gap semiconductor. These processes result in significant improvement in the conductivity of ZnO NRs and, while exposed to O<sub>2</sub> under air conditions, allow a higher density of chemisorbed oxygen ions ( $O^{2-}$ ,  $O^-$ , or  $O_2^-$ ) [26,27,65]. Another feature is that UV-viz radiation promotes the kinetics of the processes described by Equations (3) and (4) and so accelerates the recovery of the sensor resistance after the analyte input [66,67].

When ZnO absorbs UV-viz radiation, photoexcited charge carriers are generated, resulting in an activated surface state due to the dramatic increase of the concentration of free electrons, which leads to a decrease in resistance. In this highly imbalanced state, the adsorption rate of NO<sub>2</sub> increases dramatically, and the photo-adsorption rate of NO<sub>2</sub> grows as the temperature increases. The change in temperature greatly enhances the photo-adsorption of NO<sub>2</sub>, which leads to higher surface concentrations of it on the sensor surface, and as a consequence, a larger sensor signal can be achieved [68].

In order to compare the performance of ZnO/Au and ZnO/SnO<sub>2</sub> NR-based sensors with those used in the literature, we collected the data in Table 2 regarding their UV excitation with wavelengths in the range of 275–400 nm. It is worth noting that good results are observed when testing gas sensors based on In<sub>2</sub>O<sub>3</sub> [43,69,70]. However, the radiation power of LEDs used by the researchers in this work has been quite high at 5–10 mW.

**Table 2.** Summary of the performance of metal oxide gas sensors to various gases under UV activation.

Material	Analyte	Operating Temperature, °C	Response	UV Wavelength	Response Time	Reference
ZnO nanofiber	100 ppm HCHO	RT	12.6	365 nm	32 s	[71]
ZnO-SnO <sub>2</sub>	20 ppb Ozone	RT	8	325 nm	13 s	[72]
ZnO-Ag nanoparticles	5 ppm NO <sub>2</sub>	RT	1.55	470 nm	150 s	[73]
Au-modified ZnO nanowires	120 ppm ethanol	15	~1.9	370 nm	-	[74]
ZnO/Au NP	2 ppm NO <sub>2</sub>	RT	0.2	400 nm	100 s	[38]
nanoporous NiO films	4 ppm NO <sub>2</sub>	150	1	275 nm	600 s	[75]
ZnO/SnO <sub>2</sub>	10 ppm EtOH	250	10	380 nm	-	[76]
ZnO (ball milling)	100 ppm FA	RT	2.33	400 nm	-	[77]
SnO <sub>2</sub> -x	4.5 ppm EtOH	155	0.29	450 nm	-	[78]
ZnO-NP/Tb	0.1 ppm NO <sub>2</sub>	RT	54	(UV)	120 s	[79]
In <sub>2</sub> O <sub>3</sub>	1 ppm NO <sub>2</sub>	RT	60	400 nm	15 min	[43]
Polyvinylpyrrolidone/In <sub>2</sub> O <sub>3</sub>	0.5 ppm NO <sub>2</sub>	RT	1.8	325 nm	500 s	[70]
In <sub>2</sub> O <sub>3</sub> -ZnO	0.5 ppm NO <sub>2</sub>	RT	3170	365 nm	65	[69]
ZnO-Au NRs	0.5 ppm NO <sub>2</sub>	50	4.3	400 nm	744 s	This work
ZnO-Au NRs	5 ppm NO <sub>2</sub>	100	7.5	400 nm	820 s	This work
ZnO-Sn NRs	0.5 ppm NO <sub>2</sub>	50	3	400 nm	851 s	This work
ZnO-Sn NRs	5 ppm NO <sub>2</sub>	100	11.5	400 nm	1147 s	This work

When analyzing the data presented in Tables 1 and 2, it is clear that the sensors based on ZnO/Au and ZnO/SnO<sub>2</sub> NRs have advanced chemiresistive responses at an operating temperature of 50–100 °C. Calibration curves of the sensors are provided in Supplementary Materials (Figure S2). They clearly show that the sensor based on ZnO/SnO<sub>2</sub>(2) NRs has the best response. In combination with rather simple technology to modify ZnO NRs, these sensors are quite promising for many applications.

#### 4. Conclusions

In this work, arrays of ZnO NRs were synthesized on quartz substrates by the hydrothermal method and then fully characterized to extract physico-chemical, structural, electrophysical and other properties. The ZnO NRs had nearly vertical orientation, average cross-sectional sizes of 40–80 nm and lengths of 500–800 nm. To advance the functional properties of these structures, Au nanoclusters, with average sizes of  $9 \pm 1$  nm and  $4 \pm 0.5$  nm, and Sn nanoclusters, with average sizes of  $30 \pm 5$  nm and  $15 \pm 3$  nm, were formed on top of the ZnO NRs. The tin nanoclusters oxidized to tin oxide (SnO<sub>2</sub>) during a 300 °C thermal annealing. The developed sensors exhibited a high selectivity to nitrogen dioxide in concentrations of 5–50 ppm when mixed with synthetic air and exposed to an operating temperature of 200 °C. To reduce the detection limit and operating temperature, UV radiation, generated by an LED with a wavelength of 400 nm, was added. It was found that the sensors had optimal characteristics when operated under the UV and with heating in 50–150 °C range. In particular, it was shown that the ZnO/Au and ZnO/SnO<sub>2</sub> NR-based sensors detected NO<sub>2</sub> at lower concentrations of 0.5–10 ppm and had lower response times in the range of 92–389 s, which makes it possible to consider them for practice.

**Supplementary Materials:** The following supporting information can be downloaded at: <https://www.mdpi.com/article/10.3390/chemosensors11030200/s1>, Figure S1. High-resolution spectra of C1s photoelectronic lines Elemental composition of ZnO/Sn(2)—a and ZnO/Au(2)—b samples annealed at 200 and 300 °C; Figure S2. Calibration curves of NO<sub>2</sub> sensors based on ZnO/SnO<sub>2</sub> and ZnO/Au NR. Sample composition ZnO/SnO<sub>2</sub>(1)-1, ZnO/SnO<sub>2</sub>(2)-2, ZnO/Au(1)-3, ZnO/Au(2)-4; Figure S3. The contacts of zinc oxide nanorods and Au(a) and SnO<sub>2</sub> (b) nanocrystallites and the scheme of surface

potential formation on the border of ZnO/Au—(a) and ZnO/SnO<sub>2</sub> (b)—heterojunctions; Table S1. Estimation of the parameters of metal clusters on a ZnO nanorod.

**Author Contributions:** Conceptualization, V.V.P., A.P.I. and V.V.S.; methodology and project administration, V.V.P.; synthesis of films and XRD analysis, K.A.A.; XPS, S.A.K.; SEM, A.P.I.; electrophysical, gas sensitive properties and photoconductivity parameters, V.V.P., A.P.I. and A.V.N.; writing—original draft preparation, V.V.P., V.V.S., A.P.I., S.A.K. and K.A.A.; writing—review and editing, V.V.P., A.P.I. and V.V.S. All authors have read and agreed to the published version of the manuscript.

**Funding:** This study was supported by the Russian Science Foundation under grant No. 23-29-00742, <https://rscf.ru/en/project/23-29-00742/> accessed on 30 January 2023 at the Southern Federal University.

**Institutional Review Board Statement:** Not applicable.

**Informed Consent Statement:** Not applicable.

**Data Availability Statement:** Data is available from the authors on request.

**Acknowledgments:** Electrophysics and gas sensitivity measurements were conducted using equipment from the Centre for Collective Use, Microsystem Technics and Integral Sensors, Southern Federal University (SFedU). We also thank the staff of the Laboratory for the Technology of Functional Nanomaterials at the Institute of Nanotechnologies, Electronics, and Equipment Engineering (SFedU). The execution of SEM measurements and XPS analysis were supported by the Ministry of Science and Higher Education of the Russian Federation through the state task in the field of scientific activity No. FENW-2022-0001.

**Conflicts of Interest:** The authors declare no conflict of interest.

## References

1. Zhang, Y.; Jiang, Y.; Duan, Z.; Wu, Y.; Zhao, Q.; Liu, B.; Huang, Q.; Yuan, Z.; Li, X.; Tai, H. Edge-enriched MoS<sub>2</sub> nanosheets modified porous nanosheet-assembled hierarchical In<sub>2</sub>O<sub>3</sub> microflowers for room temperature detection of NO<sub>2</sub> with ultrahigh sensitivity and selectivity. *J. Hazrad. Mater.* **2022**, *434*, 128836. [[CrossRef](#)] [[PubMed](#)]
2. Gao, H.; Yu, Q.; Chen, K.; Sun, P.; Liu, F.; Yan, X.; Liu, F.; Lu, G. Ultrasensitive gas sensor based on hollow tungsten trioxide-nickel oxide (WO<sub>3</sub>-NiO) nanoflowers for fast and selective xylene detection. *J. Colloid Interface Sci.* **2019**, *535*, 458–468. [[CrossRef](#)] [[PubMed](#)]
3. Zha, X.; Xi, R.; Wu, Y.; Xu, J.; Yang, Y. Synthesis of Good Electrical Conductivity of CoCe-BTC/PEDOT for Ultrahigh Selectivity of NO<sub>2</sub> Detection. *Sensors* **2022**, *22*, 6891. [[CrossRef](#)] [[PubMed](#)]
4. Perera, A.; Madhushani, K.; Punchihewa, B.T.; Kumar, A.; Gupta, R.K. MXene-Based Nanomaterials for Multifunctional Applications. *Materials* **2023**, *16*, 1138. [[CrossRef](#)]
5. Zhao, L.; Wang, K.; Wei, W.; Wang, L.; Han, W. High-performance flexible sensing devices based on polyaniline/MXene nanocomposites. *InfoMat* **2019**, *1*, 407–416. [[CrossRef](#)]
6. Quan, W.; Shi, J.; Luo, H.; Fan, C.; Lv, W.; Chen, X.; Zeng, M.; Yang, J.; Hu, N.; Su, Y.; et al. Fully Flexible MXene-based Gas Sensor on Paper for Highly Sensitive Room-Temperature Nitrogen Dioxide Detection. *ACS Sens.* **2023**, *8*, 103–113. [[CrossRef](#)]
7. Chen, K.; Lu, H.; Li, G.; Zhang, J.; Tian, Y.; Gao, Y.; Guo, Q.; Lu, H.; Gao, J. Surface functionalization of porous In<sub>2</sub>O<sub>3</sub> nanofibers with Zn nanoparticles for enhanced low-temperature NO<sub>2</sub> sensing properties. *Sens. Actuators B Chem.* **2020**, *308*, 127716. [[CrossRef](#)]
8. Que, M.; Lin, C.; Sun, J.; Chen, L.; Sun, X.; Sun, Y. Progress in ZnO nanosensors. *Sensors* **2021**, *21*, 5502. [[CrossRef](#)]
9. Rackauskas, S.; Barbero, N.; Barolo, C.; Viscardi, G. ZnO Nanowire Application in Chemoresistive Sensing. *Nanomaterials* **2017**, *7*, 381. [[CrossRef](#)]
10. Marikutsa, A.; Novikova, A.; Romyantseva, M.; Khmelevsky, N.; Gaskov, A. Comparison of Au-functionalized semi-conductor metal oxides in sensitivity to VOC. *Sens. Actuators B Chem.* **2021**, *326*, 128980. [[CrossRef](#)]
11. Thompson, D. Using gold nanoparticles for catalysis. *Nanotoday* **2007**, *2*, 40–43. [[CrossRef](#)]
12. Xiang, D.; Liu, Z.; Wu, M.; Liu, H.; Zhang, X.; Wang, Z.; Lin, Z.W.; Li, L. Enhanced Piezo-Photoelectric Catalysis with Oriented Carrier Migration in Asymmetric Au–ZnO Nanorod Array. *Small* **2020**, *16*, 1907603. [[CrossRef](#)]
13. Bonyani, M.; Zebarjad, S.M.; Janghorban, K.; Kim, J.-Y.; Kim, H.W.; Kim, S.S. Au-Decorated Polyaniline-ZnO Electrospun Composite Nanofiber Gas Sensors with Enhanced Response to NO<sub>2</sub> Gas. *Chemosensors* **2022**, *10*, 388. [[CrossRef](#)]
14. Guo, J.; Zhang, J.; Zhu, M.; Ju, D. High-performance gas sensor based on ZnO nanowires functionalized by Au nanoparticles. *Sens. Actuators B Chem.* **2014**, *199*, 339–345. [[CrossRef](#)]
15. Franco, M.A.; Conti, P.P.; Andre, R.S.; Correa, D.S. A review on chemiresistive ZnO gas sensors. *Sens. Actuators Rep.* **2022**, *4*, 100100. [[CrossRef](#)]
16. Vuong, N.M.; Than, L.H.; Phan, T.H.; Hieu, H.N.; Nghia, N.V.; Tu, N. Ultra-Responsive and Highly Selective Ethanol Gas Sensor Based on Au Nanoparticles Embedded ZnO Hierarchical Structures. *J. Electrochem. Soc.* **2021**, *168*, 027503. [[CrossRef](#)]

17. Espid, E.; Taghipour, F. Development of highly sensitive ZnO/In<sub>2</sub>O<sub>3</sub> composite gas sensor activated by UV-LED. *Sens. Actuators B Chem.* **2017**, *241*, 828–839. [[CrossRef](#)]
18. Wei, N.; Cui, H.; Wang, X.; Xie, X.; Wang, M.; Zhang, L.; Tian, J. Hierarchical assembly of In<sub>2</sub>O<sub>3</sub> nanoparticles on ZnO hollow nanotubes using carbon fibers as templates: Enhanced photocatalytic and gas-sensing properties. *J. Colloid Interface Sci.* **2017**, *498*, 263–270. [[CrossRef](#)]
19. Choi, S.; Park, J.; Kim, S. Synthesis of SnO<sub>2</sub>–ZnO core–shell nanofibers via a novel two-step process and their gas sensing properties. *Nanotechnology* **2009**, *20*, 46. [[CrossRef](#)]
20. Li, X.; Gu, D.; Yang, Y.; Du, H.; Li, X. UV Light Activated SnO<sub>2</sub>/ZnO Nanofibers for Gas Sensing at Room Temperature. *Front. Mater.* **2019**, *6*, 158. [[CrossRef](#)]
21. Petrov, V.V.; Bayan, E.M.; Khubezhov, S.A.; Varzarev, Y.N.; Volkova, M.G. Investigation of Rapid Gas-Sensitive Properties Degradation of ZnO–SnO<sub>2</sub> Thin Films Grown on the Glass Substrate. *Chemosensors* **2020**, *8*, 40. [[CrossRef](#)]
22. Nasriddinov, A.; Romyantseva, M.; Marikutsa, A.; Gaskov, A.; Lee, J.H.; Kim, J.H.; Kim, J.Y.; Kim, S.S.; Kim, H.W. Sub-ppm Formaldehyde Detection by n-n TiO<sub>2</sub>@SnO<sub>2</sub> Nanocomposites. *Sensors* **2019**, *19*, 3182. [[CrossRef](#)] [[PubMed](#)]
23. Romyantseva, M.; Gaskov, A. Light Activation of Nanocrystalline Metal Oxides for Gas Sensing: Principles, Achievements, Challenges. *Nanomaterials* **2021**, *11*, 892.
24. Hassan, T.A.A. Enhancement of gas response of annealed ZnO film for hydrogen gas detection. *IJP* **2014**, *12*, 73–79. [[CrossRef](#)]
25. Kim, J.-H.; Sakaguchi, I.; Hishita, S.; Ohsawa, T.; Suzuki, T.T.; Saito, N. Ru-implanted WS<sub>2</sub> nanosheet gas sensors to enhance sensing performance towards CO gas in self-heating mode. *Sens. Actuators B Chem.* **2022**, *370*, 132454. [[CrossRef](#)]
26. Li, Q.H.; Wan, Q.; Liang, Y.X.; Wang, T.H. Electronic transport through individual ZnO nanowires. *Appl. Phys. Lett.* **2004**, *84*, 4556. [[CrossRef](#)]
27. Kumar, R.; Liu, X.; Zhang, J.; Kumar, M. Room-Temperature Gas Sensors Under Photoactivation: From Metal Oxides to 2D Materials. *Nano-Micro Lett.* **2020**, *12*, 164. [[CrossRef](#)]
28. Solomatin, M.A.; Glukhova, O.E.; Fedorov, F.S.; Sommer, M.; Shunaev, V.V.; Varezchnikov, A.S.; Nasibulin, A.G.; Ushakov, N.M.; Sysoev, V.V. The UV effect on the chemiresistive response of ZnO nanostructures to isopropanol and benzene at ppm concentrations in mixture with dry and wet Air. *Chemosensors* **2021**, *9*, 181. [[CrossRef](#)]
29. Ryabko, A.A.; Bobkov, A.A.; Nalimova, S.S.; Maksimov, A.I.; Levitsky, V.S.; Moshnikov, V.A.; Terukov, E.I. Gas-sensitivity of nanostructured coatings based on zinc oxide nanorods under combined activation. *TEC Phys.* **2022**, *92*, 5. [[CrossRef](#)]
30. Guarnieri, M.; Balmes, J.R. Outdoor air pollution and asthma. *Lancet* **2014**, *383*, 1581–1592. [[CrossRef](#)]
31. Barnes, P.J.; Dweik, R.A.; Gelb, A.F.; Gibson, P.G.; George, S.C.; Grasmann, H.; Pavord, I.D.; Ratjen, F.; Silkoff, P.E.; Taylor, D.R.; et al. Exhaled nitric oxide in pulmonary diseases: A comprehensive review. *Chest* **2010**, *138*, 682–692. [[CrossRef](#)]
32. Korotcenkov, G.; Cho, B. Metal oxide composites in conductometric gas sensors: Achievements and challenges. *Sens. Actuators B Chem.* **2017**, *244*, 182–210. [[CrossRef](#)]
33. Jun, J.H.; Yun, J.; Cho, K.; Hwang, I.-S.; Lee, J.-H.; Kim, S. Necked ZnO nanoparticle-based NO<sub>2</sub> sensors with high and fast response. *Sens. Actuators B Chem.* **2009**, *140*, 412–417. [[CrossRef](#)]
34. Fan, F.; Feng, Y.; Bai, S.; Feng, J.; Chen, A.; Li, D. Synthesis and Gas Sensing Properties to NO<sub>2</sub> of ZnO Nanoparticles. *Sens. Actuators B Chem.* **2013**, *185*, 377–382. [[CrossRef](#)]
35. Petrov, V.V.; Starnikova, A.P.; Abdullin, K.A.; Makarenko, D.P. Features of the mechanism of gas sensitivity of the zinc oxide nanorods arrays to carbon monoxide. *IOP Conf. Ser. J. Phys. Conf. Ser.* **2018**, *1124*, 022017. [[CrossRef](#)]
36. Petrov, V.V.; Starnikova, A.P.; Varzarev, Y.N.; Abdullin, K.A.; Makarenko, D.P. Gas sensitive properties of ZnO nanorods formed on silicon and glass substrates. *IOP Conf. Ser. Mater. Sci. Eng.* **2019**, *703*, 012038. [[CrossRef](#)]
37. Starnikova, A.; Gulyaeva, I.; Abdullin, K.; Petrov, V. Investigation of the electrophysical and gas-sensitive properties of thin nanocomposite materials based on ZnO (Sn) and ZnO (Au) nanorods NanoOstrava 2021-Nanomater. *Nanotechnol. Meet.* **2021**, *1*, 32.
38. Chakrabarty, P.; Banik, M.; Gogurla, N.; Santra, S.; Ray, S.K.; Mukherjee, R. Light trapping-mediated room-temperature gas sensing by ordered ZnO nano structures decorated with plasmonic Au nanoparticles. *ACS Omega* **2019**, *4*, 12071–12080. [[CrossRef](#)]
39. Rakshit, T.; Santra, S.; Manna, I.; Kumar, S. Enhanced sensitivity and selectivity of brush-like SnO<sub>2</sub> nanowire/ZnO nanorod heterostructure based sensors for volatile organic compounds. *RSC Adv.* **2014**, *4*, 36749. [[CrossRef](#)]
40. Su, X.; Duan, G.; Xu, Z.; Zhou, F.; Cai, W. Structure and thickness-dependent gas sensing responses to NO<sub>2</sub> under UV irradiation for the multilayered ZnO micro/nanostructured porous, thin films. *J. Colloid Interface Sci.* **2017**, *503*, 150–158. [[CrossRef](#)]
41. Lu, G.; Xu, J.; Sun, J.; Yu, Y.; Zhang, Y.; Liu, F. UV-enhanced room temperature NO<sub>2</sub> sensor using ZnO nanorods modified with SnO<sub>2</sub> nanoparticles. *Sens. Actuators B Chem.* **2012**, *162*, 82–88. [[CrossRef](#)]
42. Chinh, N.D.; Hien, T.T.; Do Van, L.; Hieu, N.M.; Quang, N.D.; Lee, S.M.; Kim, C.; Kim, D. Adsorption/desorption kinetics of nitric oxide on zinc oxide nano film sensor enhanced by light irradiation and gold-nanoparticles decoration. *Sens. Actuators B Chem.* **2019**, *281*, 262–272. [[CrossRef](#)]
43. Gonzalez, O.; Roso, S.; Vilanova, X.; Llobet, E. Enhanced detection of nitrogen dioxide via combined heating and pulsed UV operation of indium oxide nano-octahedra. *Beilstein J. Nanotechnol.* **2016**, *7*, 1507–1518. [[CrossRef](#)] [[PubMed](#)]
44. Pollack, I.B.; Lerner, B.M.; Ryerson, T.B. Evaluation of ultraviolet light-emitting diodes for detection of atmospheric NO<sub>2</sub> by photolysis-chemiluminescence. *J. Atmos. Chem.* **2010**, *65*, 111–125. [[CrossRef](#)]

45. Starnikova, A.P.; Gulyaeva, I.A.; Abdullin, K.A.; Petrov, V.V. Study of gas-sensitive properties of materials based on ZnO nanorods to nitrogen dioxide (IV). *PHENMA* **2021**, 33–34.
46. Abdullin, K.A.; Bakranov, N.B.; Ismailov, D.V.; Kalkozova, J.K.; Kumekov, S.E.; Podrezova, L.V.; Cicero, G. Composite Materials Based on Nanostructured Zinc Oxide. *Semiconductors* **2014**, *48*, 471–475. [[CrossRef](#)]
47. Gritsenko, L.V.; Abdullin, K.A.; Gabdullin, M.T.; Kalkozova, Z.K.; Kumekov, S.E.; Mukash, Z.O.; Sazonov, A.Y.; Terukov, E.I. Effect of thermal annealing on properties of polycrystalline ZnO thin films. *J. Cryst. Growth* **2017**, *457*, 164–170. [[CrossRef](#)]
48. Petrov, V.V.; Varzarev, Y.N.; Abdullin, K.A. Temperature Dependence of Electrical Properties of ZnO Nanorods Array. *IOP Conf. Ser. Mater. Sci. Eng.* **2019**, *703*, 012040. [[CrossRef](#)]
49. Petrov, V.V.; Sysoev, V.V.; Starnikova, A.P.; Volkova, M.G.; Kalazhokov, Z.K.; Storozhenko, V.Y.; Khubezhov, S.A.; Bayan, E.M. Synthesis, Characterization and Gas Sensing Study of ZnO-SnO<sub>2</sub> Nanocomposite Thin Films. *Chemosensors* **2021**, *9*, 124. [[CrossRef](#)]
50. Shalimova, K.V. *Physics of Semiconductors (Moscow: Energeia)*; Energoatomizdat: Moscow, Russia, 1976; Volume 2.
51. Starnikova, A.P.; Nesterenko, A.V.; Petrov, A.V.; Varzarev, Y.N.; Petrov, V.V. Research of the photoconductivity characteristics of thin films of complex oxides formed on non-transparent substrates. *LFPM-2021* **2021**, *2*, 125–126.
52. Petrov, V.V.; Ivanishcheva, A.P.; Volkova, M.G.; Storozhenko, V.Y.; Gulyaeva, I.A.; Pankov, I.V.; Bayan, E.M. High Gas Sensitivity to Nitrogen Dioxide of Nanocomposite ZnO-SnO<sub>2</sub> Films Activated by a Surface Electric Field. *Nanomaterials* **2022**, *12*, 2025. [[CrossRef](#)]
53. Miller, D.J.; Biesinger, M.C.; McIntyre, N.S. The interface of atomic layer deposited ZrO<sub>2</sub> on Si/SiO<sub>2</sub> from an alkoxide zirconium precursor and ethanol: A transmission electron microscopy focused study. *Surf. Interface Anal.* **2002**, *33*, 299. [[CrossRef](#)]
54. Strohmeier, B.R. An ESCA method for determining the oxide thickness on aluminum alloys. *Surf. Interface Anal.* **1990**, *15*, 51. [[CrossRef](#)]
55. Jablonski, A.; Powell, C.J. Relationships between electron inelastic mean free paths, effective attenuation lengths, and mean escape depths. *J. Electron Spectrosc. Relat. Phenom.* **1999**, *100*, 137–160. [[CrossRef](#)]
56. Fedorov, F.; Vasilkov, M.; Lashkov, A.; Varezchnikov, A.; Fuchs, D.; Kübel, C.; Bruns, M.; Sommer, M.; Sysoev, V. Toward new gas-analytical multisensor chips based on titanium oxide nanotube array. *Sci. Rep.* **2017**, *7*, 9732. [[CrossRef](#)]
57. Wei, M.; Li, C.F.; Deng, X.R.; Deng, H. Surface work function of transparent conductive ZnO films. *Energy Procedia* **2012**, *16*, 76–80. [[CrossRef](#)]
58. Mishra, Y.; Chakravadhanula, V.; Hrkac, V.; Jebiril, S.; Agarwal, D.; Mohapatra, S.; Avasthi, D.; Kienle, L.; Adelung, R. Crystal growth behaviour in Au-ZnO nanocomposite under different annealing environments and photoswitchability. *Appl. Phys.* **2012**, *112*, 064308. [[CrossRef](#)]
59. Alosfur, F.K.M.; Ridha, N.J. Synthesis, and characterization of ZnO/SnO<sub>2</sub> nanorods coreshell arrays for high performance gas sensors. *Appl. Phys. A* **2021**, *127*, 203. [[CrossRef](#)]
60. Sahm, T.; Gurlo, A.; Barsan, N.; Weimar, U. Basics of oxygen and SnO<sub>2</sub> interaction; work function change and conductivity measurements. *Sens. Actuators B Chem.* **2006**, *118*, 78–83. [[CrossRef](#)]
61. Gurlo, A. Insights into the Mechanism of Gas Sensor Operation. In *Metal Oxide Nanomaterials for Chemical Sensors*; Carpenter, M.A., Mathur, S., Kolmakov, A., Eds.; Springer: New York, NY, USA, 2013; pp. 3–34.
62. Zheng, L.; Xie, J.; Liu, X.; Yang, C.; Zheng, W.; Zhang, J. Unveiling the Electronic Interaction in ZnO/PtO/Pt Nanoarrays for Catalytic Detection of Triethylamine with Ultrahigh Sensitivity. *ACS Appl. Mater. Interfaces* **2020**, *12*, 46267–46276. [[CrossRef](#)]
63. Ma, T.; Zheng, L.; Zhao, Y.; Xu, Y.; Zhang, J.; Liu, X. Highly Porous Double-Shelled Hollow Hematite Nanoparticles for Gas Sensing. *ACS Appl. Nano Mater.* **2019**, *2*, 2347–2357.
64. Kołodziejczak-Radzimska, A.; Jesionowski, T. Zinc Oxide—From Synthesis to Application: A Review. *Materials* **2014**, *7*, 2833–2881. [[CrossRef](#)] [[PubMed](#)]
65. Hsiao, C.; Luo, L. A Rapid Process for Fabricating Gas Sensors. *Sensors* **2014**, *14*, 12219–12232. [[CrossRef](#)] [[PubMed](#)]
66. Jacobs, C.B.; Maksov, A.B.; Muckley, E.S.; Collins, L.; Mahjouri-Samani, M.; Ievlev, A.; Rouleau, C.M.; Moon, J.W.; Graham, D.E.; Sumpter, B.G.; et al. UV-activated ZnO films on a flexible substrate for room temperature O<sub>2</sub> and H<sub>2</sub>O sensing. *Sci. Rep.* **2017**, *7*, 6053. [[CrossRef](#)]
67. Joshi, N.; da Silva, L.F.; Shimizu, F.M.; Mastelaro, V.R.; M’Peko, J.C.; Lin, L.; Oliveira, O.N. UV-assisted chemiresistors made with gold-modified ZnO nanorods to detect ozone gas at room temperature. *Microchim. Acta* **2019**, *186*, 418. [[CrossRef](#)]
68. Chizhov, A.; Kutukov, P.; Gulin, A.; Astafiev, A.; Romyantseva, M. UV-Activated NO<sub>2</sub> Gas Sensing by Nanocrystalline ZnO: Mechanistic Insights from Mass Spectrometry Investigations. *Chemosensors* **2022**, *10*, 147. [[CrossRef](#)]
69. Liu, Y.; Zhang, J.; Li, G.; Liu, J.; Liang, Q.; Wang, H.; Zhu, Y.; Gao, J.; Lu, H. In<sub>2</sub>O<sub>3</sub>-ZnO nanotubes for the sensitive and selective detection of ppb-level NO<sub>2</sub> under UV irradiation at room temperature. *Sens. Actuators B* **2022**, *355*, 131322. [[CrossRef](#)]
70. Trocino, S.; Frontera, P.; Donato, A.; Bucassa, C.; Scarpino, L.A.; Antonucci, P.; Neri, G. Gas sensing properties under UV radiation of In<sub>2</sub>O<sub>3</sub> nanostructures processed by electro-spinning. *Mater. Chem. Phys.* **2014**, *147*, 35–41. [[CrossRef](#)]
71. Cui, J.; Shi, L.; Xie, T.; Wang, D.; Lin, Y. UV-light illumination room temperature HCHO gas-sensing mechanism of ZnO with different nanostructures. *Sens. Actuators B Chem.* **2016**, *227*, 220–226. [[CrossRef](#)]
72. da Silva, L.F.; M’Peko, J.C.; Catto, A.C.; Bernardini, S.; Mastelaro, V.R.; Aguir, K.; Ribeiro, C.; Longo, E. UV-enhanced ozone gas sensing response of ZnO-SnO<sub>2</sub> heterojunctions at room temperature. *Sens. Actuators B Chem.* **2017**, *240*, 573–579. [[CrossRef](#)]
73. Zhang, Q.; Xie, G.; Xu, M.; Su, Y.; Tai, H.; Du, H.; Jiang, Y. Visible light-assisted room temperature gas sensing with ZnO-Ag heterostructure nanoparticles. *Sens. Actuators B Chem.* **2018**, *259*, 269–281. [[CrossRef](#)]

74. Zou, A.L.; Qiu, Y.; Yu, J.J.; Yin, B.; Cao, G.Y.; Zhang, H.Q.; Hu, L.Z. Ethanol sensing with Au-modified ZnO microwires. *Sens. Actuators B Chem.* **2006**, *227*, 65. [[CrossRef](#)]
75. Drozdowska, K.; Welearegay, T.; Osterlund, L.; Smulko, J. Combined chemoresistive and insitu FTIR spectroscopy study of nanoporous NiO films for light-activated nitrogen dioxide and acetone gas sensing. *Sens. Actuators B Chem.* **2022**, *353*, 131125. [[CrossRef](#)]
76. Sun, J.; Liu, F.; Zhong, T.; Xu, J.; Zhang, Y.; Lu, G. Effects of UV Light Illumination on the Gas Sensing Properties of ZnO-SnO<sub>2</sub> Thick Film Sensor. *Sens. Lett.* **2011**, *9*, 824–827. [[CrossRef](#)]
77. Zou, Z.; Qiu, Y.; Xu, J.; Guo, P.; Luo, Y.; Wang, C. Enhanced formaldehyde photoelectric response on ZnO film illuminated with visible light. *J. Alloys Compd.* **2017**, *695*, 2117–2123. [[CrossRef](#)]
78. Gulyaev, A.M.; Sarach, O.B.; Kotov, V.A.; Vanin, A.A.; Anufriev, Y.V.; Konovalov, A.V. Light-enhanced sensitivity of SnO<sub>2</sub>-x gas sensors. *Semiconductors* **2008**, *42*, 726–730. [[CrossRef](#)]
79. Sayago, I.; Santos, J.P.; Sánchez-Vicente, C. The Effect of Rare Earths on the Response of Photo UV-Activate ZnO Gas. *Sensors* **2022**, *22*, 8150. [[CrossRef](#)]

**Disclaimer/Publisher's Note:** The statements, opinions and data contained in all publications are solely those of the individual author(s) and contributor(s) and not of MDPI and/or the editor(s). MDPI and/or the editor(s) disclaim responsibility for any injury to people or property resulting from any ideas, methods, instructions or products referred to in the content.